

# UC Berkeley

## UC Berkeley Previously Published Works

### Title

On the mechanics of metal imprinting by nominally flat and patterned rigid surfaces

### Permalink

<https://escholarship.org/uc/item/7xp9x475>

### Authors

Cen, J  
Komvopoulos, K

### Publication Date

2020-12-01

### DOI

10.1016/j.ijsolstr.2020.10.003

Peer reviewed



Contents lists available at ScienceDirect

## International Journal of Solids and Structures

journal homepage: [www.elsevier.com/locate/ijsoistr](http://www.elsevier.com/locate/ijsoistr)

# On the mechanics of metal imprinting by nominally flat and patterned rigid surfaces



J. Cen, K. Komvopoulos\*

Department of Mechanical Engineering, University of California, Berkeley, CA 94720, USA

## ARTICLE INFO

## Article history:

Received 22 May 2020

Received in revised form 29 August 2020

Accepted 1 October 2020

Available online 8 October 2020

## Keywords:

Deformation

Finite element analysis

Flat and patterned surfaces

Metal imprinting

Plasticity

## ABSTRACT

Basic knowledge of the deformation behavior of fabricated components is of paramount importance in materials processing. Compared to other process methods, the mechanics of metal imprinting, especially at small scales, have received relatively less research attention. However, recent demands for tuning the properties of metal surfaces by forming undulated micropatterns have spurred interest in gaining additional insight into metal imprinting. The aim of this study, therefore, was to develop effective modeling capabilities that establish a ground base for exploring the mechanics of this process. Accordingly, a finite element analysis was performed to analyze the deformation of an elastic–plastic material exhibiting isotropic strain hardening imprinted by a rigid template with a nominally flat or patterned surface. Simulation results were obtained in the form of dimensionless quantities to elucidate the effects of pattern geometry, depth of imprinting, and friction on the evolution of plasticity in the deformed material and its plastic flow behavior into the pattern cavities. In addition to insight into the mechanics of the process, this study provides a computational methodology for adjusting key design and process parameters so as to enhance the efficiency of metal imprinting.

© 2020 Elsevier Ltd. All rights reserved.

## 1. Introduction

Engraving a surface pattern on a solid body is of particular significance in several engineering and biotechnology fields, optoelectronics, haptic technology, arts, and cosmetics. One of the most common engraving processes is imprinting, also referred to as stamping when a sheet metal is forced into a rigid cavity. In this process, a rigid tool (template) is pressed against a soft substrate, causing it to plastically deform and attain a desired surface topology. Recent advances in tool patterning methods, such as lithography and chemical etching, have created opportunities for imprinting patterns of various length scales on metallic substrates, thereby modifying their surface properties and functionality. For example, the optical, friction, and gripping characteristics of a metal surface can be altered by stamping surface patterns exhibiting hierarchical architectures. It is theorized that exceptional surface properties can be obtained through functional adaptation of the surface structure at all length levels of hierarchy. However, multi-level patterning of metal surfaces by imprinting requires thorough insight into the effects of key process parameters (e.g., pattern geometry and applied pressure) and the deformation

behavior of the imprinted material on the process efficacy. Accordingly, to accomplish this objective, it is necessary to illuminate the basic mechanics of metal imprinting.

One of the commonly used methods to alter the macroscopic shape of metallic parts is metal stamping (Lim et al., 2014). The high utility of this process has motivated numerous computational studies, mainly based on the finite element method (FEM), for elucidating the intricacies of the metal stamping process. For instance, Wang and Budiansky (1978) used an FEM model to analyze sheet metal stamping by arbitrarily shaped punches and found fair agreement between numerical and experimental results for hemispherical punch stretching. Oh (1982) proposed a rigid-viscoplastic FEM formulation for metal forming analysis, while Chandra (1986) introduced an elastic-viscoplastic FEM analysis for problems involving large strains and investigated frictional effects at the punch and die interfaces on the process characteristics. Ghosh and Kikuchi (1988) presented a thermomechanical FEM analysis of sheet metal forming that uses a time-dependent elastic-viscoplastic constitutive law to model the metal flow behavior at elevated temperatures. Zimniak and Piela (2000) performed thermomechanical FEM simulations of the cup stamping process by a square punch and observed good agreement with experimental findings. Kim et al. (2001) proposed a sensitivity and optimization analysis for designing the die shape in metal stamping that is based

\* Corresponding author.

E-mail address: [kyriakos@me.berkeley.edu](mailto:kyriakos@me.berkeley.edu) (K. Komvopoulos).

on a Lagrangian formulation and reported excellent agreement with sensitivity results obtained with the finite difference method.

The use of a master surface (template) to controllably modify the microscale topology of a metal surface has been proven to be a potent technique in surface engineering (Xia and Lim, 2010). However, conversely to macroscale metal stamping, the majority of significant developments in micro/nanoscale stamping technologies, particularly imprinting, have been realized with polymeric materials. When a polymer is compressed by a hard patterned surface, the imposed deformation causes the polymer to gradually flow into the surface cavities and permanently acquire the topology imposed by the patterned surface after photo-induced curing (Traub et al., 2016). Pourdavoud et al. (2017) employed surface patterning to create nanofeatures on organo-metal halide perovskites for photonic devices. Hirai et al. (2001, 2004) studied the effects of applied pressure and height-to-volume cavity ratio on nanoimprint lithography and reported high stress concentrations at the cavity corners and an increase of the pressure needed to completely fill the cavities with increasing height-to-width cavity ratio. Zhou and Komvopoulos (2005) examined the effect of loading rate on polymer imprinting and introduced a mechanistic model that explains the viscoplastic flow of a polymer into the pattern cavities. Shiotsu et al. (2014) employed a fracture mechanics approach to study the separation of a hard mask from an imprinted polymer surface during unloading and observed friction-induced stretching of the polymer in the cavities before the instigation of interface cracking at the cavity corners, followed by crack growth along the side wall up to the top of the cavity during the detachment of the mask.

Contrary to polymeric materials, basic understanding of metal imprinting at the microscale is relatively sparse and largely empirical. Aizawa et al. (2014) devised a surface patterning method for imprinting high aspect ratio microcavities on aluminum with a diamondlike carbon-coated die and examined the effects of friction and incremental normal loading on cavity depth. Choi et al. (2017) developed an imprinting method for direct metal-to-metal patterning that uses a master stamp engraved with square nickel micropillars to form submicron square cavities on electrochemically polished pure aluminum at room temperature. Yamamoto and Kuwabara (2008) developed a form rolling process for imprinting microgrooves onto metal surfaces and reported high pattern transcription quality. La et al. (2020) developed a metal-to-metal micro/nanoscale imprinting process that utilizes heat to augment the pattern transcription onto a metal substrate. In addition to experimental studies, numerical analyses have also been performed to provide insight into the mechanics of the imprinting

process at small scales. Riccardi and Montanari (2004) used an FEM model to analyze the indentation of an elastic–perfectly plastic material by a flat cylindrical rigid punch and observed the development of high stresses and plastic strains at the punch edge, a rapid stress decay with increasing distance from the contact edge, and the formation of plastic shear bands at  $45^\circ$  from the surface plane. These investigators also examined the evolution of the plastic zone below the rigid indenter and the formation of a pile-up for a strain hardening material and the effect of friction on the normal force. Komvopoulos and Choi (1992) investigated the interaction of the stress fields generated in an elastic semi-infinite solid by a rigid surface consisting of an array of spherical protrusions and predicted a critical distance below which the effect of neighboring deformation becomes significant. In a series of contact mechanics studies of elastic–plastic patterned media, Gong and Komvopoulos (2004a,b) examined the effect of the pattern geometry on the resulting deformation and stress fields and the propensity for crack initiation due to mechanical and thermal (friction) surface tractions. Xu et al. (2014) used the FEM to study the compression of isotropic hardening aluminum by a flat punch and reported the development of high stresses at the contact edge, extending into the substrate at  $45^\circ$  from the surface normal.

The objective of the present study was to provide a comprehensive mechanics analysis of metal imprinting and obtain solutions of important process parameters in dimensionless form. Using a rigid, flat surface as the control geometry, the effects of surface pattern geometry (i.e., shape, size, and spacing of surface protrusions), coefficient of friction, and penetration depth on the normal force, energy dissipation, and plastic flow behavior of an elastic–plastic substrate material exhibiting isotropic strain hardening were examined in the context of finite element simulations. The numerical results presented below illuminate the importance of the plastic flow behavior of the deformed material in metal imprinting and pave the way for further extending this modeling work to examine other important effects, such as more complex pattern geometries, oscillatory movement at the template/substrate interface, frictional heating, substrate temperature, and other stress–strain constitutive laws.

## 2. Simulation procedure

### 2.1. Finite element modeling

Fig. 1 shows the quartered FEM model of a flat substrate ( $w \times t \times l = 150 \times 300 \times 200 \mu\text{m}$ ) and a flat punch (template) ( $a = b = c = 50 \mu\text{m}$ ) with vertical ( $\theta = 90^\circ$ ) side walls. Due to

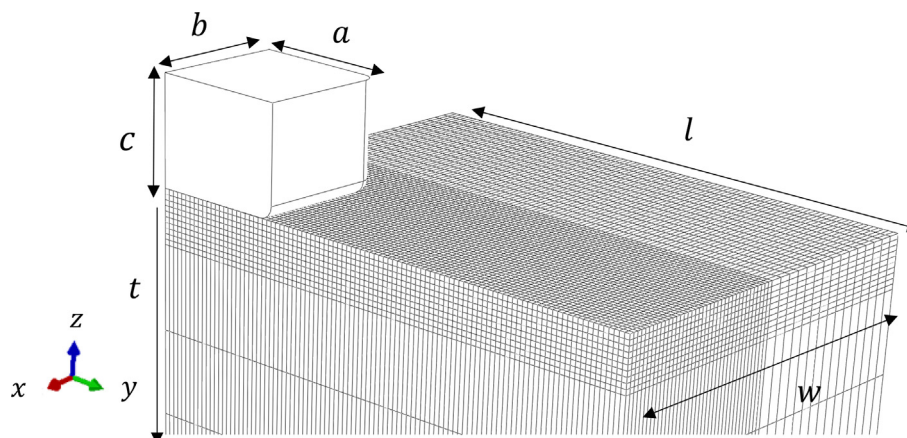


Fig. 1. Finite element mesh of a substrate in contact with a flat surface.

symmetry, only a quarter of the contact geometry needs to be analyzed. The template edges are rounded off to a radius of curvature equal to 5 μm to prevent the excessive distortion of adjacent substrate elements during the deformation and also because ideally sharp corners are unrealistic. The nodes at the bottom boundary of the mesh ( $z = -t$ ) are fully constrained, whereas the nodes at the left ( $y = 0$ ) and right ( $y = l$ ) boundaries are fixed in the  $y$ -direction. To account for the large strain gradients in the vicinity of the contact interface, the mesh adjacent to the template/substrate interface is refined with 2-μm-size elements. To enhance the computational efficiency, the near-surface mesh that does not come into contact with the template is refined with 4-μm-size elements, whereas the bulk of the substrate is meshed with 20-μm-size elements. The substrate is discretized by 100,700 8-node cubic elements with 109,080 nodes, of which 50% are allocated to the surface regions, whereas 5942 10-node tetrahedral elements with 9071 nodes are used to mesh the flat template.

Surface contact is simulated with a finite sliding algorithm that treats the deformable substrate and the rigid surface as slave and master surfaces, respectively, and controls the relative separation and slip between the interacting surfaces. When a slave node comes into contact anywhere along the master surface, it is constrained to slide along that surface by the algorithm, which tracks the position of the slave node relative to the master surface during contact deformation. The finite sliding algorithm was implemented in the present FEM analysis by means of automatically generated contact elements. At each integration point of a contact element, the overclosure was adjusted to inhibit that point on the deforming surface from penetrating the rigid surface and the relative shear slip was computed afterwards.

To determine an appropriate mesh refinement, the plane-strain contact problem of a rigid flat punch in frictionless normal contact with an elastic half-space discretized by various mesh sizes was analyzed and numerical solutions of the contact pressure distribution were compared with the analytical solution given by (Johnson, 1985)

$$p(y) = \frac{P}{\pi a} \left[ 1 - \left( \frac{y}{a} \right)^2 \right]^{-1/2}, \tag{1}$$

where  $P$  is the normal force per unit length in the  $x$ -direction and  $y$  is the distance from the center of contact. Fig. 2 shows a comparison between FEM results of the contact pressure distribution at  $x = 0$  for refined meshes adjacent to the substrate surface with an element size equal to 2 and 4 μm and the analytical solution for  $P = 0.1$  N/m and substrate elastic modulus and Poisson's ratio equal to 70 GPa and 0.35, respectively. The good agreement of the variation of the contact pressure with the dimensionless distance  $\bar{y} = y/a$

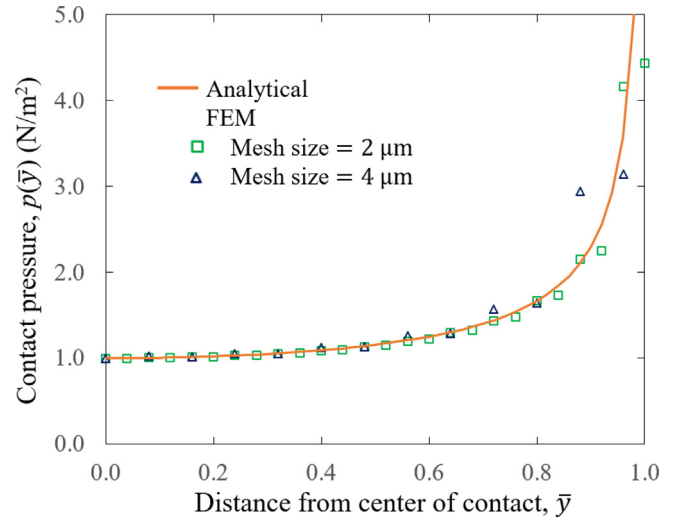


Fig. 2. Comparison of analytical (Hertz) and FEM solutions of the contact pressure distribution along the plane of symmetry ( $x = 0$ ) for an elastic substrate compressed by a rigid flat punch.

obtained with the two FEM meshes and the theoretical solution validates the selection of a refined mesh with 2-μm-size elements and confirms the applicability of the modeling assumptions.

Fig. 3 shows the FEM model of a patterned template ( $b \times c \times l = 50 \times 40 \times 200 \mu\text{m}$ ) with protrusion edges rounded off to a radius of curvature equal to 5 μm in contact with the same substrate as that shown in Fig. 1. Because the  $x = 0$  plane is a symmetry plane, only half of the contact geometry has to be modeled. Because the objective was to analyze the effect of neighboring protrusions on the deformation behavior, only a unit cell of the geometry is modeled, i.e., one protrusion between two half-width protrusions. The patterned template is meshed with ~20,000 10-node tetrahedral elements having 29,598 nodes. Likewise with the flat template/substrate model, the pure master-slave option is used to simulate surface contact. Similar to the previous FEM model, the nodes at the left ( $y = 0$ ) and right ( $y = l$ ) boundaries of the mesh are fixed in the  $y$ -direction, whereas the nodes at the bottom boundary of the mesh ( $z = -t$ ) are fully constrained.

All of the FEM simulations were performed in displacement-control mode, i.e., the indenting rigid template was quasistatically advanced towards the stationary substrate up to a maximum normal displacement  $d = 10$  and 15 μm for the nominally flat and patterned templates in approximately 70 and 120 increments, respectively. Table 1 gives the magnitudes of geometric parameters and the coefficient of friction  $\mu$  at the template/substrate con-

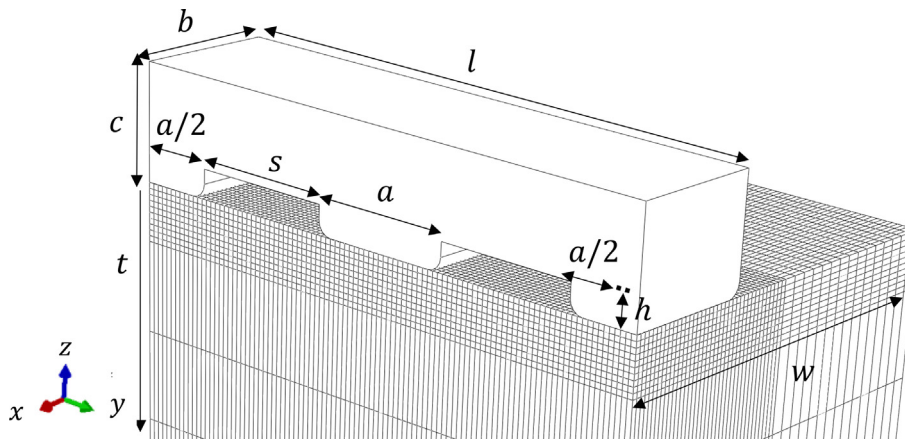


Fig. 3. Finite element mesh of a substrate in contact with a patterned surface.

tact interface used in the analysis. All of the FEM simulations were performed with the multi-physics code ABAQUS/Standard (implicit solver).

2.2. Elastic-plastic material behavior

The substrate is modelled as an isotropic strain hardening material obeying the following constitutive law

$$\sigma = E\varepsilon \quad (\sigma < \sigma_Y), \tag{2a}$$

$$\sigma = K\varepsilon^n \quad (\sigma \geq \sigma_Y), \tag{2b}$$

where  $\sigma$  is the true stress,  $\varepsilon$  is the true strain,  $E$  is the elastic modulus,  $\sigma_Y$  is the yield strength,  $K$  is the strength coefficient, and  $n$  is the strain hardening exponent. The mechanical properties of the substrate given in Table 2 are typical of aluminum (Rashad et al., 2015). The strain hardening exponent  $n$  was assumed to be equal to the ultimate strain  $\varepsilon_u$ . Consequently, the strain hardening coefficient was computed in terms of the ultimate strength  $\sigma_u$  and corresponding ultimate strain  $\varepsilon_u$  by  $K \approx \sigma_u/\varepsilon_u^n$ .

Yielding is determined by the von Mises yield criterion, given by

$$\sigma_{eq} = \left(\frac{3}{2}S_{ij}S_{ij}\right)^{1/2} = \sigma_Y, \tag{3}$$

where  $\sigma_{eq}$  is the von Mises equivalent stress and  $S_{ij}$  are components of the deviatoric stress tensor.

The evolution of plasticity is traced by the equivalent plastic strain  $\varepsilon_{eq}^p$ , given by

$$\varepsilon_{eq}^p = \int_{\Omega} \left(\frac{2}{3}d\varepsilon_{ij}^p d\varepsilon_{ij}^p\right)^{1/2}, \tag{4}$$

where  $\Omega$  is the strain path used to track the accumulation of plasticity and  $d\varepsilon_{ij}^p$  denotes plastic strain increments.

2.3. Dimensionless parameters

To present general solutions, the input and output parameters of the analysis are normalized by appropriate quantities. Thus, the dimensionless von Mises equivalent stress and equivalent plastic strain are defined by  $\bar{\sigma}_{eq} = \sigma_{eq}/\sigma'_Y$  and  $\bar{\varepsilon}_{eq}^p = \varepsilon_{eq}^p/\varepsilon_{max}^p$ , where  $\sigma'_Y$  is the current yield strength (i.e., the stress at the current strain on the strain hardening curve) and  $\varepsilon_{max}^p$  is the maximum plastic strain at the current step. In addition, the dimensionless normal force and elastic, plastic, and friction energies are given by  $\bar{P} = P/(A_a\sigma'_Y)$ ,  $\bar{W}_e = W_e/W$ ,  $\bar{W}_p = W_p/W$ , and  $\bar{W}_f = W_f/W$ , respectively, where  $A_a$  is the apparent contact area and  $W$  is the total work. Finally, the dimensionless normal displacement, protrusion spacing, max-

**Table 1**  
Geometrical parameters and coefficient of friction used in the FEM simulations.

Indentation depth of a flat surface, $d$	10 $\mu\text{m}$
Indentation depth of a patterned surface, $d$	15 $\mu\text{m}$
Side wall angle, $\theta$	60°, 75°, 90°
Protrusion lateral distance, $s$	25, 50, 75 $\mu\text{m}$
Protrusion width, $a$	50 $\mu\text{m}$
Protrusion height, $h$	10 $\mu\text{m}$
Coefficient of friction, $\mu$	0.1, 0.5, 0.7

**Table 2**  
Mechanical properties of the substrate material.

Elastic modulus $E$ (GPa)	Yield strength $\sigma_Y$ (MPa)	Yield strain $\varepsilon_Y$	Poisson's ratio $\nu$	Ultimate strength $\sigma_u$ (MPa)	Ultimate strain $\varepsilon_u$	Strain hardening coefficient $K$ (MPa)	Strain hardening exponent $n$	Fracture strain $\varepsilon_f$
70	57	0.014	0.35	105	0.115	135	0.115	0.18

imum equivalent plastic strain, and fraction of cavity area (volume) filled by the substrate material are defined by  $\bar{d} = d/a$  (flat template surface) or  $d/h$  (patterned template surface),  $\bar{s} = s/a$ ,  $\bar{\varepsilon}_{eq,max}^p = \varepsilon_{eq,max}^p/\varepsilon_f$ , and  $\bar{a} = A'_c/A_c$ , respectively, where  $\varepsilon_f$  is the fracture strain,  $A'_c$  is the cross-sectional cavity area filled by the deformed substrate material, and  $A_c$  is the apparent cross-sectional area of the cavity.

3. Results and discussion

3.1. Imprinting by a flat template surface

Fig. 4 shows isostress contours of the dimensionless equivalent plastic strain  $\bar{\varepsilon}_{eq}^p$  and von Mises equivalent stress  $\bar{\sigma}_{eq}$  before and after full unloading for  $\theta = 90^\circ$ ,  $\bar{d} = 0.25$ , and  $\mu = 0.1$ . The large plastic strains at the contact edge and especially the corners of the residual impression (Fig. 4(a)) are due to the high stress concentrations at these regions (Fig. 4(b)), which produce large stress and strain gradients at the perimeter of the impression. The development of high stresses at the contact edge and corners of the impression is consistent with the analytical and FEM results shown in Fig. 2. High stresses at the contact edge developed with the instigation of loading and spread into the substrate at 45° from

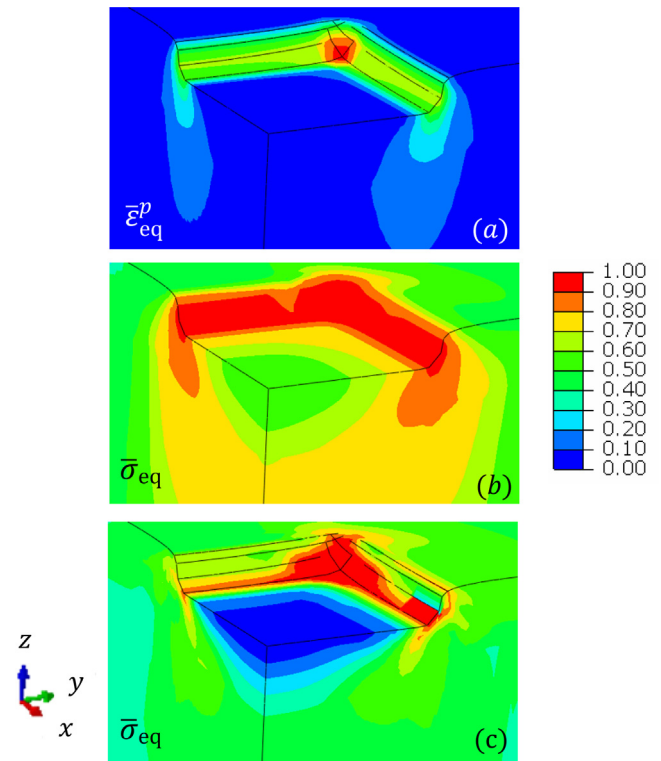


**Fig. 4.** Dimensionless strain and stress results for an elastic-plastic substrate indented by a rigid flat surface ( $\theta = 90^\circ$ ,  $\bar{d} = 0.25$ , and  $\mu = 0.1$ ): (a) equivalent plastic strain  $\bar{\varepsilon}_{eq}^p$ ; (b) von Mises equivalent stress  $\bar{\sigma}_{eq}$ , and (c) residual von Mises equivalent stress  $\bar{\sigma}_{eq}$  after full unloading.

the surface normal as the load was increased, consistent with other studies (Riccardi and Montanari, 2004; Xu et al., 2014), causing severe plastic shearing of the substrate material against the edge and side walls of the rigid template. When the template was withdrawn, the plastic zone around the impression inhibited the full release of the elastic strain energy accumulated in the surrounding elastic zone, resulting in high localized residual stresses at the edge and corners of the impression and material pile-up around the impression (Fig. 4(c)). High residual stresses can significantly affect the mechanical behavior of the imprinted material (Xing and Lu, 2004) and degrade the quality of the imprinted surface in subsequent material processing (e.g., deburring and planarization). The pile-up geometry is controlled by the plastic flow of material around the contact edge and against the side walls of the flat template.

Fig. 5 shows the variation of the dimensionless normal force  $\bar{P}$  with the dimensionless normal displacement  $\bar{d}$  and side wall angle  $\theta$  for  $\mu = 0.1$ . The force response reveals a two-stage deformation behavior influenced by the plastic flow of material adjacent to the template surface and the side wall angle. The linear increase

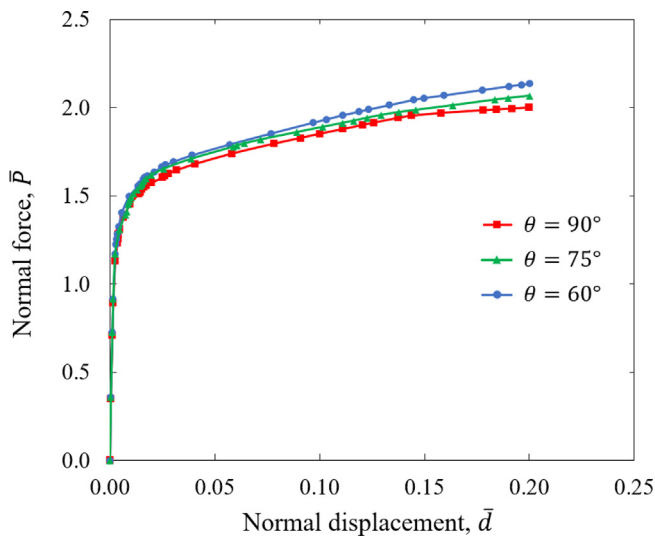


Fig. 5. Dimensionless normal force  $\bar{P}$  versus dimensionless normal displacement  $\bar{d}$  for an elastic–plastic substrate indented by a rigid flat surface ( $\theta = 60^\circ, 75^\circ,$  and  $90^\circ$  and  $\mu = 0.1$ ).

of the normal force in the first deformation stage is illustrative of the elastic behavior of the deformed substrate. In the second deformation stage, the contact force increases gradually with the progression of plasticity in the vicinity of the template front. The deformation in this stage is characterized by the flow of material first sideways and then upwards, resulting in plastic shearing against the template’s edge and side walls and the formation of a pile-up. Thus, the force response in this deformation stage is predominantly controlled by plastic flow in the substrate and the template geometry. The latter effect is evidenced from the fact that the side wall angle affects the normal force only in the second deformation stage when the formation of a pile-up becomes pronounced. The increase of the normal force with decreasing side wall angle is attributed to the growth of the contact area due to the interaction of the pile-up material with the sloped side wall. The smaller the side wall angle, the larger the increase of the contact area due to the pile-up effect and, consequently, the higher the normal force to further deform the material. Because this effect was not observed with vertical side walls ( $\theta = 90^\circ$ ), the normal force for  $\theta = 90^\circ$  is solely due to the plastic flow of the material.

### 3.2. Imprinting by a patterned template surface

Fig. 6 shows isostress contours of the dimensionless von Mises equivalent stress  $\bar{\sigma}_{eq}$  at the symmetry plane ( $x = 0$ ) of the substrate due to surface imprinting by a rigid patterned template versus the dimensionless normal displacement  $\bar{d}$  for  $\theta = 90^\circ, \bar{s} = 1.0,$  and  $\mu = 0.1$ . In the early stage of imprinting (Fig. 6(a)), the deformation below the protrusions of the patterned template is similar to that of the flat template (Fig. 4(b)), i.e., high stresses are localized at the protrusion edge and corners. However, as the imprinting process proceeds, the substrate material begins to flow into the cavities between the protrusions and the high stress pockets expand in the  $45^\circ$  direction below the contact surface (Fig. 6(b)), eventually joining each other to form a high stress band below each protrusion (Fig. 6(c)). After the patterned template is retracted, high residual stresses are produced in the near-surface region of the substrate just below the contact interface (Fig. 6(d)), in profound difference with the residual stress field generated by the flat template (Fig. 4(c)).

Further insight into the deformation induced by the patterned template surface can be obtained in the light of the distribution of the dimensionless equivalent plastic strain  $\bar{\epsilon}_{eq}^p$  at the symmetry

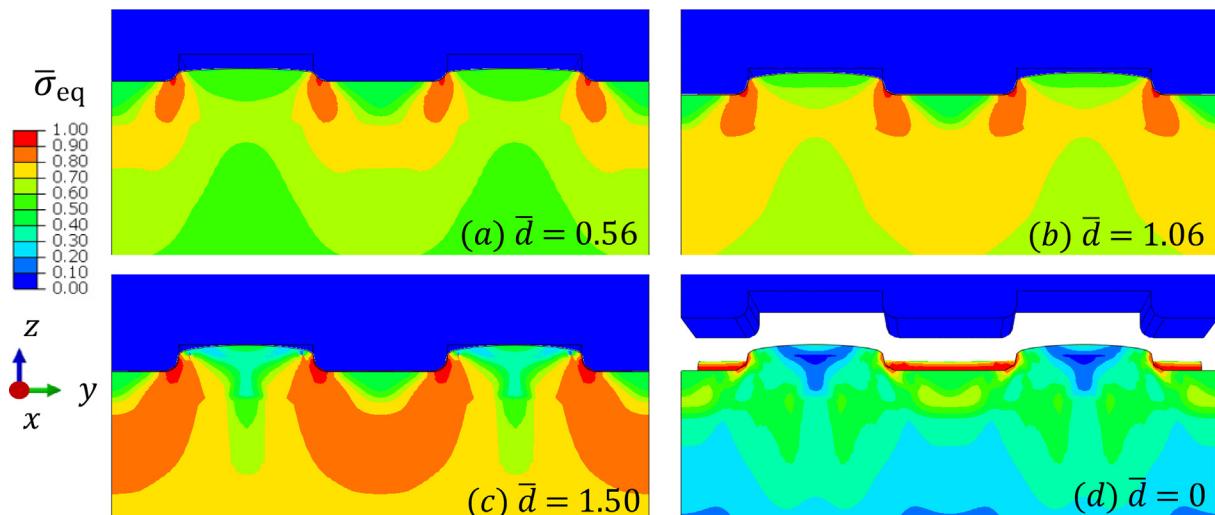


Fig. 6. Distribution of dimensionless von Mises equivalent stress  $\bar{\sigma}_{eq}$  in the plane of symmetry ( $x = 0$ ) for an elastic–plastic substrate indented by a rigid patterned surface ( $\theta = 90^\circ, \bar{s} = 1.0,$  and  $\mu = 0.1$ ): (a)  $\bar{d} = 0.56,$  (b)  $\bar{d} = 1.06,$  (c)  $\bar{d} = 1.50,$  and (d)  $\bar{d} = 0$  (fully unloaded).

plane ( $x = 0$ ) of the substrate (Fig. 7(a)) and the isometric overview of the deformed substrate (Fig. 7(b)) for  $\theta = 90^\circ$ ,  $\bar{d} = 1.50$ ,  $\bar{s} = 1.0$ , and  $\mu = 0.1$ . Likewise the flat template, the highest plastic strains are localized at the protrusion corners of the patterned template, where excessive plastic shearing occurs as the material is forced into the cavities (Fig. 7(b)). The foregoing deformation may lead to material transfer at those regions of excessive plastic shearing, contaminating the template surface and, consequently, degrading the imprinting quality. Fig. 7(c) shows the variation of the dimensionless maximum equivalent plastic strain  $\bar{\epsilon}_{eq,max}^p$  with the dimensionless normal displacement  $\bar{d}$  for flat and patterned template surfaces,  $\theta = 90^\circ$ , and  $\mu = 0.1$ . While the slope of the  $\bar{\epsilon}_{eq,max}^p$  curve of the patterned surface is initially larger than that of the flat surface, for a dimensionless normal displacement of the patterned surface  $\bar{d} > 1.0$ , the two curves exhibit equal slopes, implying similar deformation behavior. This trend is attributed to the progressive filling of the cavities, eventually leading to a patterned surface behavior similar to that of the flat surface. However, as shown in Fig. 7(a), complete filling of the cavities does not occur due to the existing geometric constraints and the plastic flow of the material, consistent with the findings of a previous study (Hirai et al., 2001). Nevertheless, it will be shown later that the fraction of unfilled cavity volume is small. Therefore, it may be inferred that for relatively large normal displacements the deformation behavior of the patterned template approximates that of the flat template.

It is noted that the equivalent plastic strain contours shown in Fig. 4(a) and 7 reveal the development of large plastic strain gradients in the vicinities of the substrate adjacent to the corners of the

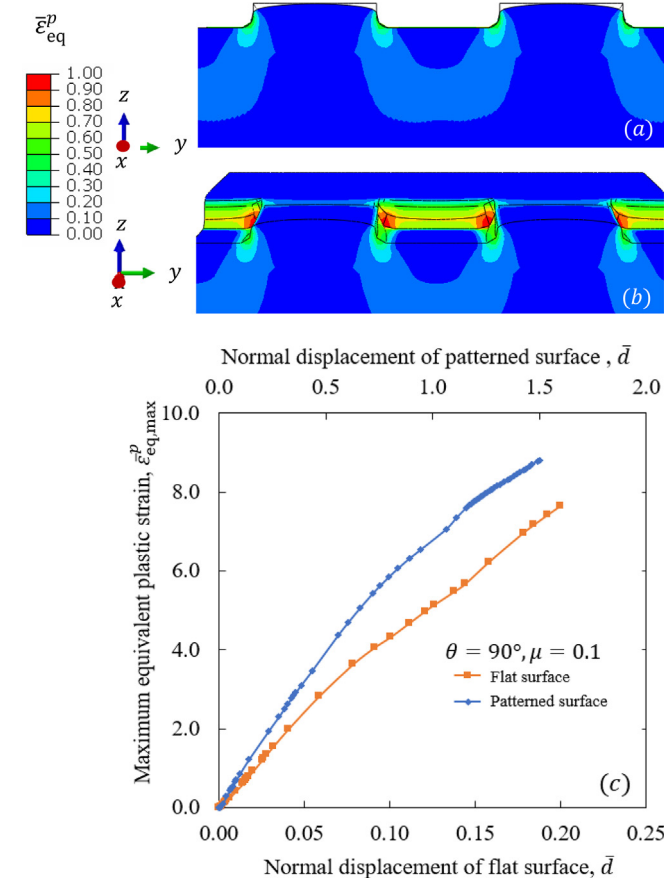


Fig. 7. Distribution of dimensionless equivalent plastic strain  $\bar{\epsilon}_{eq}^p$  for  $\bar{d} = 1.50$  (a) at the plane of symmetry ( $x = 0$ ) and (b) in isometric view, and (c) dimensionless maximum equivalent plastic strain  $\bar{\epsilon}_{eq,max}^p$  versus dimensionless normal displacement  $\bar{d}$  for an elastic-plastic substrate indented by a rigid patterned surface ( $\theta = 90^\circ$ ,  $\bar{s} = 1.0$ , and  $\mu = 0.1$ ).

rigid template, which act as stress raiser points. The constitutive laws used in conventional plasticity theory, such as that used in the present analysis, do not include size effects. In microscale plasticity, however, metallic materials that are nonuniformly deformed into the plastic regime may exhibit a strong size effect, whereby the smaller the size the stronger the material response. This has led to the development of various theories of strain gradient plasticity, which employ an internal material length scale to account for size effects in microscale plastic deformation (Fleck and Hutchinson, 1993; Fleck et al., 1994; Abu Al-Rub and Voyiadjis, 2004; Chakravarthy and Curtin, 2011). The present analysis can be extended to include size effects encountered at micron and sub-micron scales in metal imprinting by implementing in the analysis a constitutive law in which the yield stress exhibits a dependence on both strain and strain gradient.

The deformation behavior of the patterned template surface can be further interpreted in terms of the energy characteristics of the problem at hand. Fig. 8 shows the dimensionless elastic, plastic, and frictional work  $\bar{W}_e$ ,  $\bar{W}_p$ , and  $\bar{W}_f$ , respectively, versus the dimensionless normal displacement  $\bar{d}$  for  $\theta = 90^\circ$ ,  $\bar{s} = 1.0$ , and  $\mu = 0.1$ . As expected, the dominant deformation mode during the initial stage of imprinting is elastic. However, a sharp transition from elastic to plastic dominated deformation commences at a very small normal displacement ( $\bar{d} \approx 0.02$ ), beyond which the elastic and plastic works exhibit opposite trends. Thus, the elastic and plastic works demonstrate two-stage variation. The initial rapid increase of the plastic work is attributed to the accumulation of plasticity at the protrusion edges and corners, whereas the subsequent gradual increase is associated with the progressive filling of the cavities. In fact, the slope of the plastic work stabilizes at  $\bar{d} \approx 0.8$ , consistent with the constant slope of  $\bar{\epsilon}_{eq,max}^p$  for  $\bar{d} \geq 1.0$  (Fig. 7(c)). The extremely low frictional work dissipation is due to the low coefficient of friction ( $\mu = 0.1$ ) and indicates the dominance of plasticity in imprinting processes involving low-friction and/or well-lubricated template/substrate material systems demonstrating low adhesion (Komvopoulos, 2012). Another factor contributing to the very low frictional work is that relative slip at the template/substrate interface is mostly confined over a very small fraction of the contact area at the protrusion edges, partly due to the vertical side walls ( $\theta = 90^\circ$ ), where localized excessive shearing guides the material into the cavities (Figs. 7(a) and 7(b)).

Fig. 9 illustrates the effect of the coefficient of friction on the imprinting behavior of a patterned template surface for  $\theta = 90^\circ$  and  $\bar{s} = 1.0$ . The force-displacement response shown in Fig. 9(a) reveals several important trends. First, the normal force is marginally affected by the variation of the coefficient of friction. This seemingly counterintuitive effect can be explained by considering

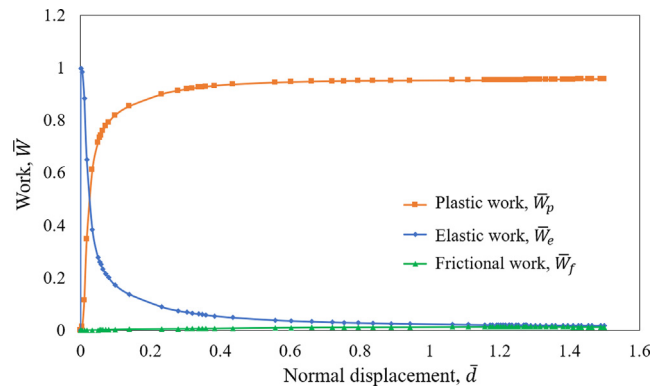
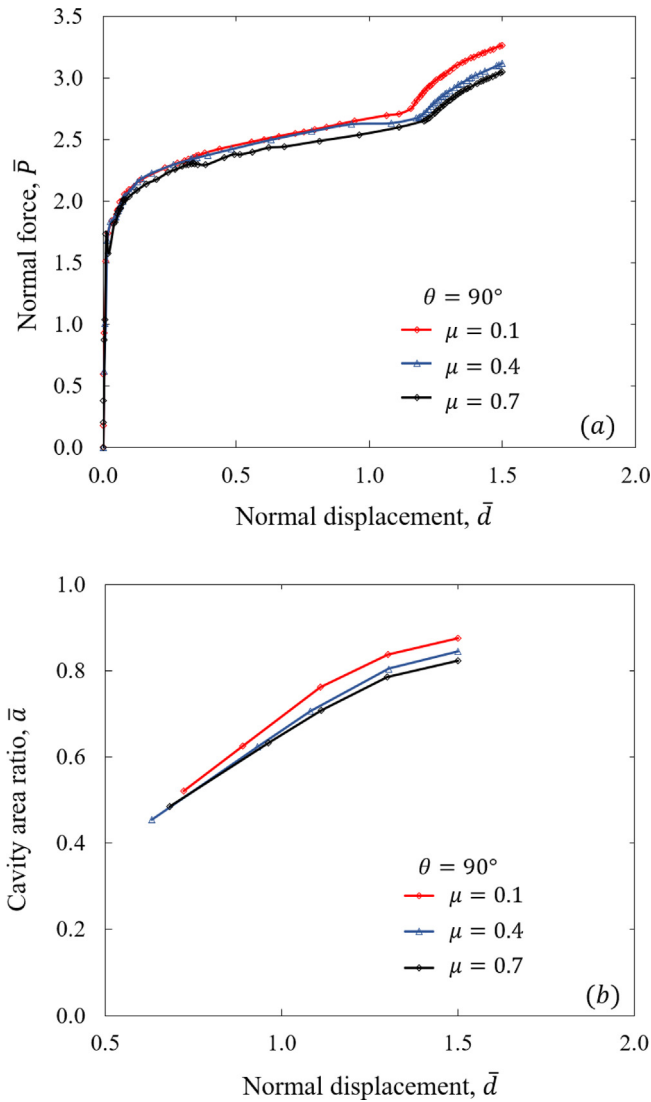


Fig. 8. Dimensionless elastic, plastic, and frictional work  $\bar{W}_e$ ,  $\bar{W}_p$ , and  $\bar{W}_f$ , respectively, versus dimensionless normal displacement  $\bar{d}$  for an elastic-plastic substrate indented by a rigid patterned surface ( $\theta = 90^\circ$ ,  $\bar{s} = 1.0$ , and  $\mu = 0.1$ ).



**Fig. 9.** (a) Dimensionless normal force  $\bar{P}$  and (b) cavity area ratio  $\bar{a}$  versus dimensionless normal displacement  $\bar{d}$  for an elastic–plastic substrate indented by a rigid patterned surface ( $\theta = 90^\circ$ ,  $\bar{s} = 1.0$ , and  $\mu = 0.1, 0.4$ , and  $0.7$ ).

the effect of friction on the contact intimacy at the template/substrate interface. For a given normal displacement, the contact area decreases with the increase of coefficient of friction because friction impedes the plastic flow of material and, consequently, filling of the template cavities. This is evidenced from the fact that the friction effect becomes notable only in the second stage of the imprinting process where the cavities are significantly filled with plastically deformed material. Thus, the slightly higher normal force for lower coefficient of friction is attributed to the establishment of a relatively larger contact area (due to the effect of cavity filling), requiring a higher normal force to further advance the template into the substrate. A second important observation is that the force–displacement response demonstrates a profound change in both slope and linearity at  $\bar{d} \approx 1.2$ , implying a marked change in contact geometry, which is attributed to the substantial filling of the cavities. Indeed, as shown in Fig. 9(b), the cavity area ratio  $\bar{a}$  increases above  $\sim 0.8$  in the dimensionless normal displacement range  $\bar{d} \geq 1.2$ , with the rate of cavity filling and force slope both decreasing in this range. A third observation from Fig. 9(b) is that higher friction leads to less cavity filling, consistent with the indirect effect of the coefficient of friction on the normal force through

the contact area discussed earlier. Evidently, as the contact area increases with the proliferation of cavity filling, a larger force is needed to push the template into the substrate. The gradual saturation of cavity filling is demonstrated by the progressively decreasing slope of the cavity area ratio with increasing normal displacement (Fig. 9(b)).

Another important factor of the imprinting process is the lateral distance of the pattern protrusions. Fig. 10 shows isostress contours of the dimensionless von Mises equivalent stress  $\bar{\sigma}_{eq}$  for  $\bar{d} = 0.5 - 1.5$ ,  $\bar{s} = 0.5 - 1.5$ ,  $\theta = 90^\circ$ , and  $\mu = 0.1$ . The results reveal stress intensification with increasing normal displacement and decreasing protrusion lateral distance due to the strengthening interaction of the stress fields of neighboring protrusions. Consequently, the highest stresses in the substrate arise for  $\bar{d} = 1.5$  and  $\bar{s} = 0.5$  (Fig. 10(c)). However, for relatively small normal displacement and large protrusion spacing, the neighboring deformation effect becomes secondary and the stress field below each protrusion resembles that of a flat punch. Since the foregoing situation is observed for  $\bar{d} = 0.5$  and  $\bar{s} = 1.5$  (Fig. 10(g)), it may be inferred that for patterned surfaces with protrusions spaced apart by distances of  $\geq 1.5$  times the protrusion width, the stress field below each protrusion is independent of the spatial distribution of the protrusions, consistent with the findings of another study (Komvopoulos and Choi, 1992). The interaction of the stress fields of neighboring protrusions can be further interpreted by considering the plastic flow of material flowing into the cavities. The protrusion distance controls the cavity volume and, in turn, the degree of cavity filling by plastically deformed material. Thus, for a small protrusion distance (e.g.,  $\bar{s} = 0.5$ ), the small cavity volume leads to premature filling, and the stress field remote from the template/substrate contact interface becomes uniform (Fig. 10(c)) similar to that of the flat surface.

The variation of the dimensionless normal force  $\bar{P}$  and cavity area ratio  $\bar{a}$  with the dimensionless normal displacement  $\bar{d}$ , shown in Figs. 11(a) and 11(b), respectively, provides further insight into the protrusion spacing effect on the imprinting process. For a small protrusion distance (i.e.,  $\bar{s} = 0.5$ ), the force–distance response is similar to that of the flat surface (Fig. 5), suggesting a secondary effect of protrusion spacing on global parameters, such as the normal force. However, larger protrusion distances (i.e.,  $\bar{s} = 1.0$  and  $1.5$ ) not only increase proportionally the normal force but also induce a transition to a rapidly intensifying force at  $\bar{d} \approx 1.0 - 1.2$ . The sharp force increase beyond this critical normal displacement is attributed to the pronounced effect of cavity filling, which depends on the protrusion distance. As shown in Fig. 11(b), the filling rate of the cavities is significantly affected by the protrusion distance. While the filling of smaller cavities ( $\bar{s} = 0.5$ ) increases moderately with the normal displacement, the larger cavities are filled up much faster, approaching saturation for  $\bar{d} > 1.5$ . Thus, the increase of the normal force with the protrusion distance may be associated with the concomitant increase of the real contact area and the more prominent strain hardening due to the enhancement of material plastic shearing inside the larger cavities.

The transcription of the template geometry onto the substrate surface can be discussed in the context of the cavity area ratio results shown in Figs. 9(b) and 11(b). While increasing the normal displacement augments the replication of the template geometry on the imprinted surface, increasing the coefficient of friction and/or decreasing the protrusion spacing yields an opposite effect. This can be explained by considering the effect of friction on the plastic shear resistance of material sliding against the template surface and the dependence of cavity volume on the protrusion distance discussed above. Specifically, higher friction hinders material flow into the cavities, whereas a smaller protrusion

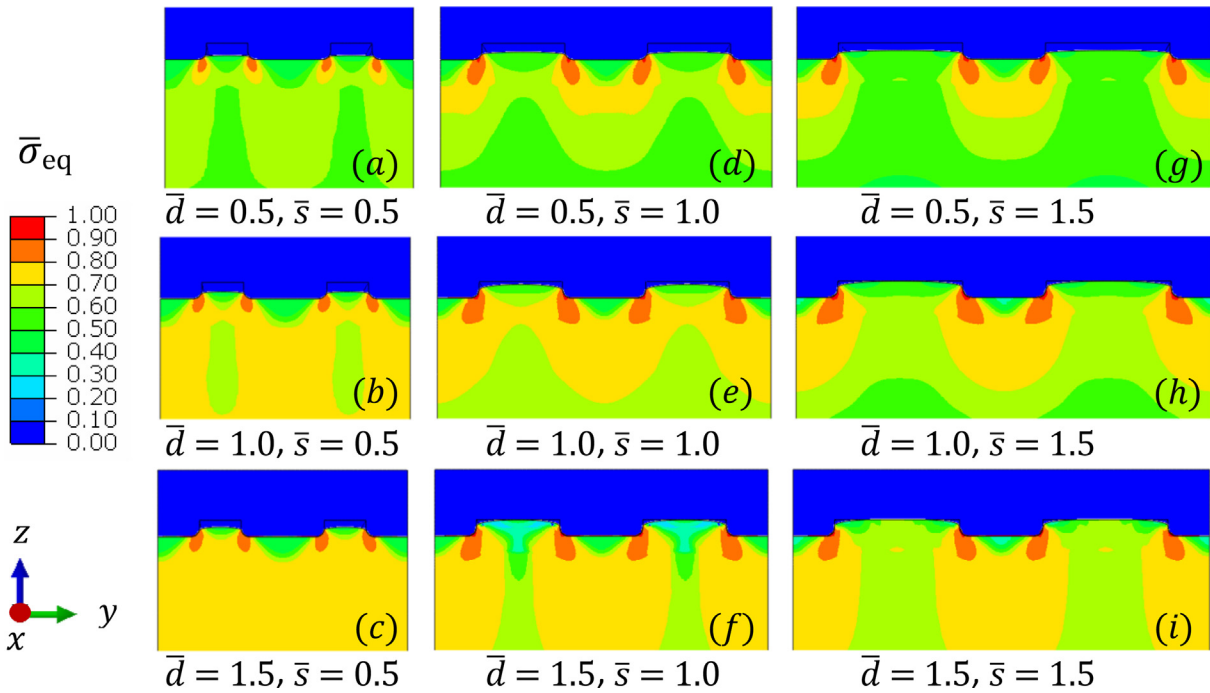


**Fig. 10.** Distribution of dimensionless von Mises equivalent stress  $\bar{\sigma}_{eq}$  in the plane of symmetry ( $x = 0$ ) for an elastic–plastic substrate indented by a rigid patterned surface ( $\theta = 90^\circ$  and  $\mu = 0.1$ ): (a)  $\bar{d} = 0.5$  and  $\bar{s} = 0.5$ , (b)  $\bar{d} = 1.0$  and  $\bar{s} = 0.5$ , (c)  $\bar{d} = 1.5$  and  $\bar{s} = 0.5$ , (d)  $\bar{d} = 0.5$  and  $\bar{s} = 1.0$ , (e)  $\bar{d} = 1.0$  and  $\bar{s} = 1.0$ , (f)  $\bar{d} = 1.5$  and  $\bar{s} = 1.0$ , (g)  $\bar{d} = 0.5$  and  $\bar{s} = 1.5$ , (h)  $\bar{d} = 1.0$  and  $\bar{s} = 1.5$ , and (i)  $\bar{d} = 1.5$  and  $\bar{s} = 1.5$ .

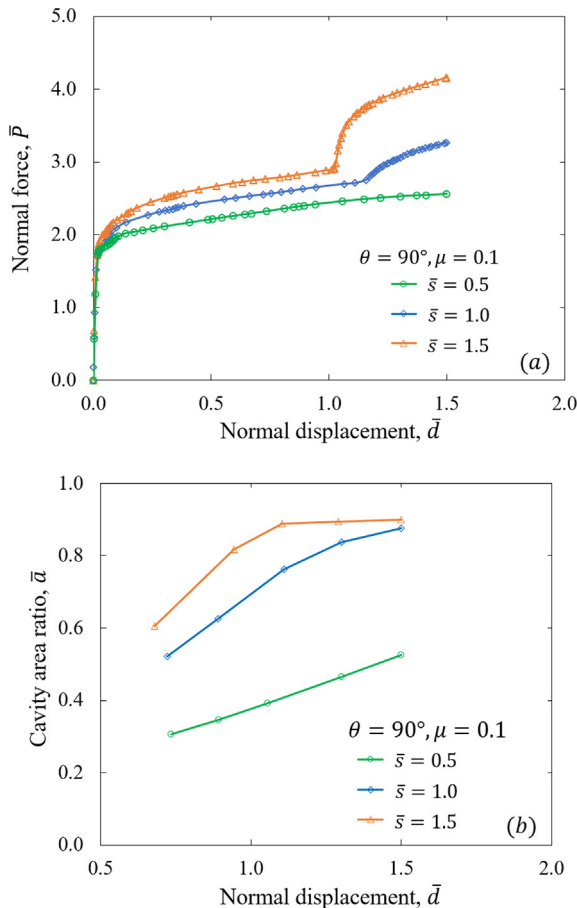


**Fig. 11.** (a) Dimensionless normal force  $\bar{P}$  and (b) cavity area ratio  $\bar{a}$  versus dimensionless normal displacement  $\bar{d}$  for an elastic–plastic substrate indented by a rigid patterned surface ( $\theta = 90^\circ$ ,  $\bar{s} = 0.5, 1.0$ , and  $1.5$ , and  $\mu = 0.1$ ).

distance reduces the free space for upward moving plastic material. These results suggest that coating the template surface with a lubricious film that reduces the adhesion of the interacting surfaces by increasing the material incompatibility (Komvopoulos, 2012) or by applying heat to enhance the flow ability of the substrate material by lowering its yield strength may greatly enhance the imprinting process.

Fig. 12 shows the effect of the protrusion lateral distance (or cavity volume) on the variation of the dimensionless maximum equivalent plastic strain  $\bar{\epsilon}_{eq,max}^p$  with the dimensionless normal displacement  $\bar{d}$  for  $\theta = 90^\circ$  and  $\mu = 0.1$ . A solution of the flat surface is also shown for comparison. The increase of  $\bar{\epsilon}_{eq,max}^p$  with  $\bar{s}$  is consistent with the force results shown in Fig. 11(a), that is, for fixed  $\bar{d}$ ,  $\bar{\epsilon}_{eq,max}^p$  increases with  $\bar{s}$ . Moreover, as the normal displacement increases, the slopes of the strain curves of the patterned surface approach that of the flat surface, consistent with the similar deformation behaviors of patterned and flat surfaces observed at relatively large normal displacements.

In addition to metal imprinting, the present analysis has direct implications in other fields where knowledge of the mechanics of a patterned surface compressing a metallic surface is critical to the optimization of the material process. An illustrative example of an important application area is ultrasonic wire bonding, an indispensable method for manufacturing interconnects in the semiconductor industry (Long et al., 2017). In this process, a bonding tool with a patterned surface (typically V-shaped or nominally flat with a surface micropattern) is used to grip onto a bonding wire of a soft metal like copper or aluminum. The oscillation of the patterned tool against the metal wire under an applied load causes plastic flow of the wire into the tool cavities, establishing a strong grip which is critical to subsequent plastic shearing of the wire against the substrate to form a strong bond. Therefore, the quality of the bond depends strongly on the normal force, oscillation amplitude, and plastic flow of the metal wire into the tool cavities. The numerical methodology developed in

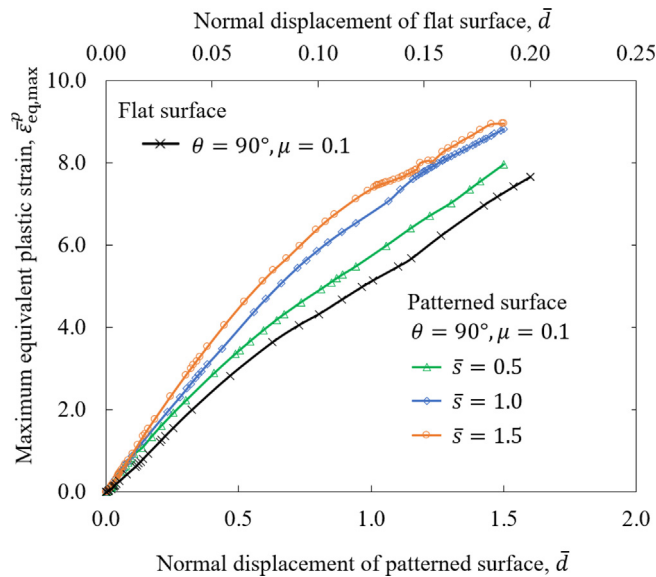


**Fig. 12.** Dimensionless maximum equivalent plastic strain  $\bar{\epsilon}_{eq,max}^{pp}$  versus dimensionless normal displacement  $\bar{d}$  for an elastic-plastic substrate indented by a rigid flat or patterned surface ( $\theta = 90^\circ$ ,  $\bar{s} = 0.5, 1.0$ , and  $1.5$ , and  $\mu = 0.1$ ).

this study can be easily extended to include oscillation at the template/substrate interface, heating due to sliding friction, energy dissipation in the form of plastic deformation and substrate heating, or even other types of constitutive stress-strain laws. A comprehensive analysis of the foregoing effects should be invaluable to the design of more efficient tools for metal imprinting and for optimizing the process via tactical tuning of key parameters. The effect of the oscillatory motion of a patterned template on the deformation behavior of a metallic substrate will be examined in a forthcoming publication.

#### 4. Conclusions

The mechanics of metal imprinting by nominally flat and patterned surfaces was examined in the light of FEA simulations. A parametric analysis of numerical results in dimensionless form was used to elucidate the effects of surface pattern parameters on the mechanical behavior of the plastically deformed substrate material. In the case of flat-surface imprinting, high stresses and strains develop at the contact edge and corners of the rigid template, where the material exhibits excessive shearing and strain hardening. The evolution of the normal force comprises two deformation stages: an initial predominantly elastic response characterized by a large slope and a steady-state response dominated by plasticity where the normal force increases gradually with the progression of deformation. The effect of the side wall angle becomes pronounced with the advancement of plasticity, with a smaller side wall angle producing a higher normal force due to the development of a larger contact area. Although a similar deformation pattern is observed in the case of patterned-surface imprinting during the initial stage of deformation, i.e., high stress and strain concentrations at the edges and corners of the pattern protrusions, the deformation behavior is significantly affected by the evolution of plasticity that intensifies the interaction of neighboring stress/strain fields and increases the plastic flow of material into the cavities. This results in a three-stage force response, with the first two stages showing similarity with those of the flat surface and the third stage characterized by the sharp increase of the normal force caused by cavity filling that increases the contact area significantly.

The normal force, cavity filling, and intensity of stress/strain fields increase with increasing protrusion distance and decreasing coefficient of friction. At large normal displacements (i.e., advanced cavity filling), the maximum equivalent plastic strain in the material adjacent to the protrusion edges and corners and the subsurface stress field in the substrate approach those of flat-surface imprinting. The results of this study provide insight into the effects of significant design and material parameters in metal imprinting and establish a modeling framework for investigating other important effects, such as oscillation and frictional heating at the template/substrate interface, more complex pattern geometries, and other constitutive models.

#### Declaration of Competing Interest

The authors declare that they have no known competing financial interests or personal relationships that could have appeared to influence the work reported in this paper.

#### References

- Abu Al-Rub, R.K., Voyiadjis, G.Z., 2004. Analytical and experimental determination of the material intrinsic length scale of strain gradient plasticity theory from micro- and nano-indentation experiments. *Int. J. Plast.* 20, 1139–1182.
- Aizawa, T., Tamaki, M., Fukuda, T., 2014. Large area micro-texture imprinting onto metallic sheet via CNC stamping. *Procedia Eng.* 81, 1427–1432.
- Chakravarty, S.S., Curtin, W.A., 2011. Stress-gradient plasticity. *Proc. Nat. Acad. Sci. USA* 108, 15716–15720.
- Chandra, A., 1986. A generalized finite element analysis of sheet metal forming with an elastic-viscoplastic material model. *ASME J. Eng. Ind.* 108, 9–15.
- Choi, J.-Y., Ko, Y.B., Kim, J., Yoon, G.S., Park, J., Heo, Y.M., La, M., 2017. Direct metal to metal imprinting for developing 1-step manufacturing process of patterned metal surface. *Procedia Eng.* 207, 1022–1026.
- Fleck, N.A., Hutchinson, J.W., 1993. A phenomenological theory for strain gradient effects in plasticity. *J. Mech. Phys. Solids* 41, 1825–1857.
- Fleck, N.A., Muller, G.M., Ashby, M.F., Hutchinson, J.W., 1994. Strain gradient plasticity: theory and experiment. *Acta Metall. Mater.* 42, 475–487.
- Ghosh, S., Kikuchi, N., 1988. Finite element formulation for the simulation of hot sheet metal forming processes. *Int. J. Eng. Sci.* 26, 143–161.
- Gong, Z.-Q., Komvopoulos, K., 2004a. Mechanical and thermomechanical elastic-plastic contact analysis of layered media with patterned surfaces. *ASME J. Tribol.* 126, 9–17.
- Gong, Z.-Q., Komvopoulos, K., 2004b. Surface cracking in elastic-plastic multi-layered media due to repeated sliding contact. *ASME J. Tribol.* 126, 655–663.
- Hirai, Y., Fujiwara, M., Okuno, T., Tanaka, Y., Endo, M., Irie, S., Nakagawa, K., Sasago, M., 2001. Study of the resist deformation in nanoimprint lithography. *J. Vac. Sci. Technol. B* 19, 2811–2815.
- Hirai, Y., Konishi, T., Yoshikawa, T., Yoshida, S., 2004. Simulation and experimental study of polymer deformation in nanoimprint lithography. *J. Vac. Sci. Technol. B* 22, 3288–3293.
- Johnson, K.L., 1985. *Contact Mechanics*. Cambridge University Press, Cambridge, UK.
- Kim, N.H., Choi, K.K., Chen, J.S., 2001. Die shape design optimization of sheet metal stamping process using meshfree method. *Int. J. Numer. Methods Eng.* 51, 1385–1405.
- Komvopoulos, K., 2012. Adhesive wear. In: R.W. Bruce (Ed.), *Handbook of Lubrication and Tribology, Volume II: Theory and Design*, second ed., CRC Press, Boca Raton, FL, Chapter 7, pp. 7-1–7-21.
- Komvopoulos, K., Choi, D.-H., 1992. Elastic finite element analysis of multi-asperity contacts. *ASME J. Tribol.* 114, 823–831.
- La, M., Hwang, T.Y., Choi, J.-Y., Hong, S., Park, S.J., Kang, J., Choi, D., 2020. Development of a metal-to-metal imprinting process: transcription quality analysis and surface wettability characterization. *Appl. Surf. Sci.* 527, 146823.
- Lim, Y., Venugopal, R., Ulsay, A.G., 2014. *Process Control for Sheet-Metal Stamping: Process Modeling, Controller Design and Shop-Floor Implementation*. Springer-Verlag, London, UK.
- Long, Y., Twiefel, J., Wallaschek, J., 2017. A review on the mechanisms of ultrasonic wedge-wedge bonding. *J. Mater. Process. Technol.* 245, 241–258.
- Oh, S.I., 1982. Finite element analysis of metal forming processes with arbitrarily shaped dies. *Int. J. Mech. Sci.* 24, 479–493.
- Pourdavoud, N., Wang, S., Mayer, A., Hu, T., Chen, Y., Marianovich, A., Kowalsky, W., Heiderhoff, R., Scheer, H.-C., Riedl, T., 2017. Photonic nanostructures patterned by thermal nanoimprint directly into organo-metal halide perovskites. *Adv. Mater.* 29, 1605003.
- Rashad, M., Pan, F., Yu, Z., Asif, M., Lin, H., Pan, R., 2015. Investigation on microstructural, mechanical and electrochemical properties of aluminum composites reinforced with graphene nanoplatelets. *Prog. Nat. Sci. Mater. Int.* 25, 460–470.
- Riccardi, A., Montanari, R., 2004. Indentation of metals by a flat-ended cylindrical punch. *Mater. Sci. Eng. A* 381, 281–291.

- Shiotsu, T., Uemura, K., Tochino, T., Ooi, S., Onishi, Y., Yasuda, M., Kawata, H., Kobayashi, T., Hirai, Y., 2014. Simulation of the template release process based on fracture mechanics in nanoimprint lithography. *Microelectron. Eng.* 123, 105–111.
- Traub, M.C., Longsine, W., Truskett, V.N., 2016. Advances in nanoimprint lithography. *Annu. Rev. Chem. Biomol. Eng.* 7, 583–604.
- Yamamoto, M., Kuwabara, T., 2008. Micro form rolling: imprinting ability of microgrooves on metal shafts. *J. Mater. Process. Technol.* 201, 232–236.
- Wang, N.-M., Budiansky, B., 1978. Analysis of sheet metal stamping by a finite-element method. *ASME J. Appl. Mech.* 45, 73–82.
- Zimniak, Z., Piela, A., 2000. Finite element analysis of a tailored blanks stamping process. *J. Mater. Process. Technol.* 106, 254–260.
- Zhou, J., Komvopoulos, K., 2005. Nanoconfinement effect on the mechanical behavior of polymer thin films. *Proc. Mater. Res. Soc. Symp.* 880E, BB4.3.1–BB4.3.6.
- Xia, Y., Lim, B., 2010. Beyond the confines of templates. *Nature* 467, 923–924.
- Xing, Y.M., Lu, J., 2004. An experimental study of residual stress induced by ultrasonic shot peening. *J. Mater. Process. Technol.* 152, 56–61.
- Xu, A., Vodenitcharova, T., Kabir, K., Flores-Johnson, E.A., Hoffman, M., 2014. Finite element analysis of indentation of aluminium foam and sandwich panels with aluminium foam core. *Mater. Sci. Eng. A* 599, 125–133.